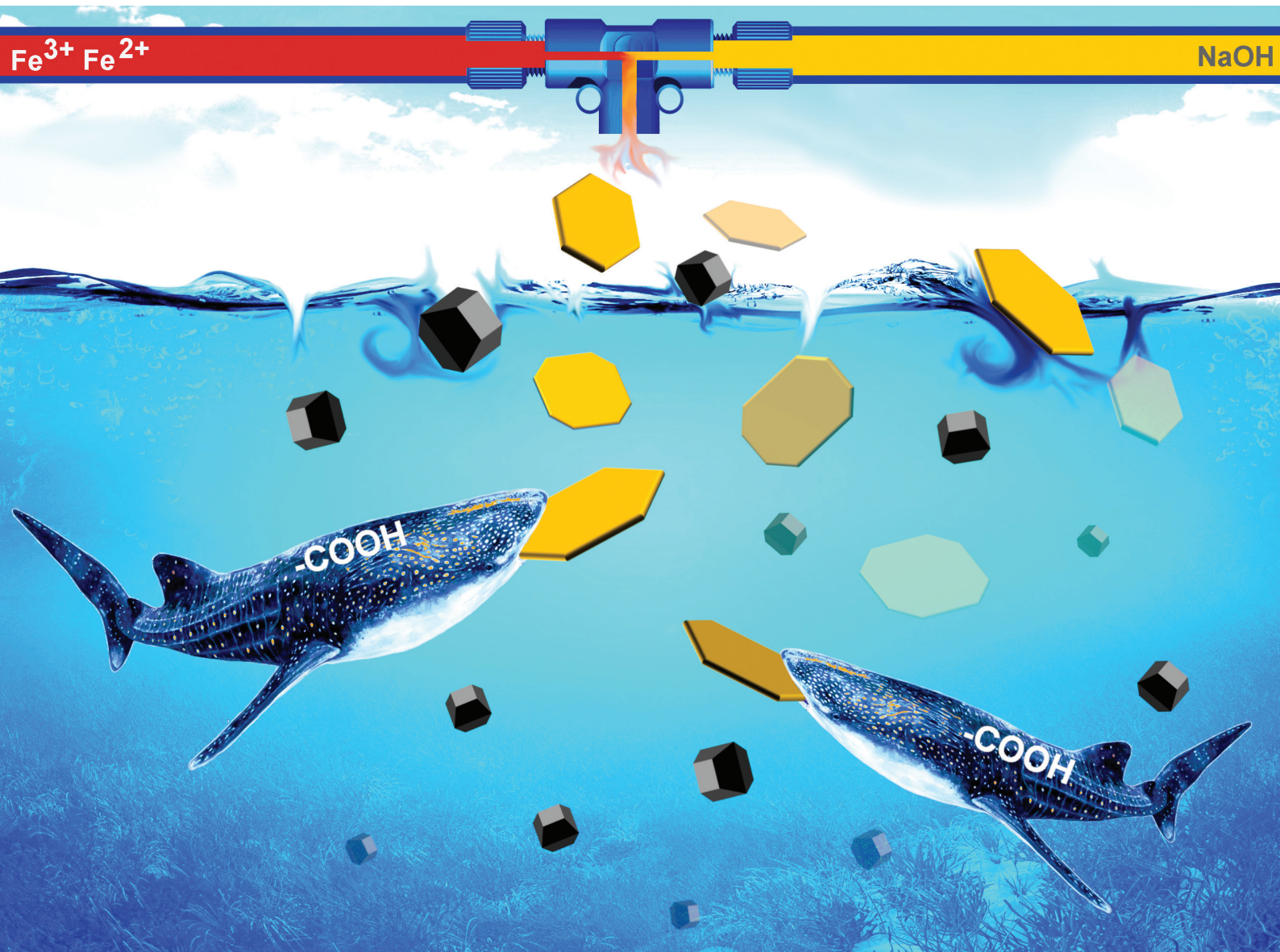


# Nanoscale

[rsc.li/nanoscale](https://rsc.li/nanoscale)



ISSN 2040-3372

## PAPER

Nguyen Thi Kim Thanh, Asterios Gavriilidis *et al.*  
Small iron oxide nanoparticles as MRI  $T_1$  contrast agent:  
scalable inexpensive water-based synthesis using a flow  
reactor



Cite this: *Nanoscale*, 2021, **13**, 8795

## Small iron oxide nanoparticles as MRI $T_1$ contrast agent: scalable inexpensive water-based synthesis using a flow reactor†

Maximilian O. Besenhard,<sup>a</sup> Luca Panariello,<sup>a</sup> Céline Kiefer,<sup>b</sup> Alec P. LaGrow,<sup>c</sup> Liudmyla Storozhuk,<sup>d</sup> Francis Perton,<sup>b</sup> Sylvie Begin,<sup>b</sup> Damien Mertz,<sup>b</sup> Nguyen Thi Kim Thanh<sup>b\*</sup> and Asterios Gavriilidis<sup>a\*</sup>

Small iron oxide nanoparticles (IONPs) were synthesised in water via co-precipitation by quenching particle growth after the desired magnetic iron oxide phase formed. This was achieved in a millifluidic multi-stage flow reactor by precisely timed addition of an acidic solution. IONPs ( $\leq 5$  nm), a suitable size for positive  $T_1$  magnetic resonance imaging (MRI) contrast agents, were obtained and stabilised continuously. This novel flow chemistry approach facilitates a reproducible and scalable production, which is a crucial paradigm shift to utilise IONPs as contrast agents and replace currently used Gd complexes. Acid addition had to be timed carefully, as the inverse spinel structure formed within seconds after initiating the co-precipitation. Late quenching allowed IONPs to grow larger than 5 nm, whereas premature acid addition yielded undesired oxide phases. Use of a flow reactor was not only essential for scalability, but also to synthesise monodisperse and non-agglomerated small IONPs as (i) co-precipitation and acid addition occurred at homogenous environment due to accurate temperature control and rapid mixing and (ii) quenching of particle growth was possible at the optimum time, *i.e.*, a few seconds after initiating co-precipitation. In addition to the timing of growth quenching, the effect of temperature and dextran present during co-precipitation on the final particle size was investigated. This approach differs from small IONP syntheses in batch utilising either growth inhibitors (which likely leads to impurities) or high temperature methods in organic solvents. Furthermore, this continuous synthesis enables the low-cost (<£10 per g) and large-scale production of highly stable small IONPs without the use of toxic reagents. The flow-synthesised small IONPs showed high  $T_1$  contrast enhancement, with transversal relaxivity ( $r_2$ ) reduced to  $20.5\text{ mM}^{-1}\text{ s}^{-1}$  and longitudinal relaxivity ( $r_1$ ) higher than  $10\text{ mM}^{-1}\text{ s}^{-1}$ , which is among the highest values reported for water-based IONP synthesis.

Received 8th February 2021,  
Accepted 11th March 2021

DOI: 10.1039/d1nr00877c  
[rsc.li/nanoscale](http://rsc.li/nanoscale)

## Introduction

The current interest for novel positive ( $T_1$ ) contrast agents for magnetic resonance imaging (MRI) arises from the health risks posed by the current clinical choices, *i.e.*, gadolinium complexes.<sup>1</sup> Iron oxide nanoparticles (IONPs) are a potential

substitute, as they are biocompatible with several FDA approved products<sup>2–4</sup> and high  $T_1$  values (*i.e.*, long times till the longitudinal magnetisation regrows to its maximum value before an MRI pulse) have been observed for exceedingly small particles.<sup>5–8</sup>

The promising  $T_1$  performance of small IONPs ( $\leq 5$  nm) is due to their high surface-to-volume ratio increasing the exposure of surface Fe ions to the surrounding water/hydrogen.<sup>6,9,10</sup> In contrast to IONPs used for  $T_2$  contrast enhancement, their performance is not dominated by the high magnetic moment. The exact mechanism controlling  $T_1$  performance is still not clear, but may rely on the accessibility of water molecules to surface iron ions similarly to Gd complexes. Despite their desirable characteristics, the reproducible and scalable production of biocompatible small IONPs remains challenging.<sup>6,11,12</sup>

Thermal decomposition syntheses, where organic iron precursors are heated above 200 °C in high boiling point organic

<sup>a</sup>Department of Chemical Engineering, University College London, London, WC1E 7JE, UK. E-mail: [a.gavriilidis@ucl.ac.uk](mailto:a.gavriilidis@ucl.ac.uk)

<sup>b</sup>Institut de Physique et Chimie des Matériaux de Strasbourg, BP 43, 67034 Strasbourg, France

<sup>c</sup>International Iberian Nanotechnology Laboratory, Braga 4715-330, Portugal

<sup>d</sup>Biophysics group, Department of Physics and Astronomy, University College London, London, WC1E 6BT, UK. E-mail: [ntk.thanh@ucl.ac.uk](mailto:ntk.thanh@ucl.ac.uk)

<sup>†</sup>UCL Healthcare Biomagnetic and Nanomaterials Laboratories, 21 Albemarle Street, London, W1S 4BS, UK

Electronic supplementary information (ESI) available. See DOI: [10.1039/d1nr00877c](https://doi.org/10.1039/d1nr00877c)



solvents can provide highly monodisperse IONPs with diameters significantly below 5 nm and excellent  $T_1$  performance.<sup>13–20</sup> When targeting biomedical applications, however, the involved reagents, by-products, and organic solvents present challenges. For example, labour and cost-intensive post-processing are required, such as a time-consuming ligand exchange step, to render the IONPs dispersible in aqueous solution. For polyol methods, however, ligand exchange has been achieved *via* simple experimental protocols.<sup>11</sup>

Water-based precipitation methods, such as co-precipitation (CP) methods<sup>21</sup> or the oxidation of initially precipitated ferrous hydroxides<sup>22</sup> are more desirable from a regulatory perspective, but provide limited control of particle formation dynamics, hence, IONP size. Still, the synthesis of small IONPs *via* aqueous precipitation methods was demonstrated recently, as described below. The common method to synthesise small IONPs is the addition of chelating ions<sup>23</sup> or macromolecules such as dextran (which likely yields agglomerates with a reduced surface area),<sup>7,24</sup> frequently in combination with the initiation of CP, *i.e.*, mixing of the precursor and base solution, at high temperatures<sup>25</sup> followed by a controlled cooling.<sup>26,27</sup> Also, fast mixing has been shown to promote the synthesis of small IONPs.<sup>28–30</sup> Alternatively, small IONPs for MRI can be produced *via* rapid (microwave) heating of a  $\text{FeCl}_3$  and trisodium citrate solution together with the reducing agent hydrazine.<sup>31,32</sup>

The route for IONP  $T_1$  contrast agents to reach market maturity is long and brings challenges, not only for chemists, but also engineers and entrepreneurs. It is well understood that only synthetic protocols yielding high performance contrast agents without using scarce, expensive, or toxic reagents/additives are worth considering. The scalability of a synthesis is pivotal too.

Scale-up is commonly considered as the logical step following the proof of principle, but up-scaling of lab procedures is frequently very challenging. Hence scalability and pilot production (at rates way below full-scale production) have been identified as key issues in bringing research across the so called “Valley of Death” (the gap between research and commercialisation) in high-cost, and high-risk areas such as nanotechnology.<sup>33,34</sup>

In this work, we present a novel synthesis of small IONPs utilising flow chemistry. Flow reactors have been widely used for nanoparticle synthesis<sup>35–38</sup> including IONPs<sup>39–43</sup> as they are advantageous for fast mixing, precise temperature control, and can operate continuously, providing opportunities for large-scale production. We demonstrate how these advantages, in conjunction with closely timed reagent addition to quench particle growth just after the formation of the most magnetic iron oxide phase (the inverse spinel structure of magnetite  $\text{Fe}_3\text{O}_4$  and/or maghemite  $\gamma\text{-Fe}_2\text{O}_3$ ), lead to small IONPs with good  $T_1$  performance at large scale using aqueous syntheses.

In the following, we show how the presence of dextran, alteration of the quenching time and of the reaction temperature affect the flow synthesis, discuss the exact quenching mechanism and the IONP  $T_1$  contrast agent potential.

## Materials and methods

### Solution preparation

Following our previous procedure,<sup>44</sup> a 0.1 M Fe precursor solution was prepared by dissolving ferrous and ferric chlorides in a 1 : 2  $\text{FeCl}_2\cdot 4\text{H}_2\text{O}$  :  $\text{FeCl}_3\cdot 6\text{H}_2\text{O}$  molar ratio in deionised (DI) water (resistivity  $\geq 15 \text{ M}\Omega \text{ cm}$ ), yielding a  $\text{pH}_{\text{precursor}}$  of 1.8. For studies using dextran ( $M_w \sim 6000 \text{ g mol}^{-1}$ ), the equivalent of one  $\text{H}(\text{C}_6\text{H}_{10}\text{O}_5)$  unit per Fe was added to the precursor solution. The precursor solution was prepared freshly for each experiment. As base solution served a 0.57 M NaOH solution prepared from 2 M NaOH stock solution and DI water. For growth quenching and stabilisation (as discussed later) a 0.32 M citric acid (CA) solution, with a  $\text{pH}_{\text{CA}}$  of 1.8, was used. Details of all chemicals used including product numbers are provided in the electronic supplementary information (ESI), see Table S1.†

### IONP flow synthesis

**Step 1: Initiation of co-precipitation.** Following previous flow reactor designs<sup>44,45</sup> a syringe pump was used to pump the base and precursor solution (after preheating to the reaction temperature) through a first T-mixer. The flow rates used of 5 ml  $\text{min}^{-1}$  (each) allowed for fast mixing, *i.e.*, mixing times  $<50$  ms for the standard reaction temperature of 60 °C.<sup>45</sup>

**Step 2: Quenching and stabilisation.** Previous studies showed that feeding the right amount of an acidic solution after IONP growth was completed (100 s after initiating CP) can de-agglomerate the clustered structures formed during CP and stabilise the IONPs.<sup>44</sup> This successful de-agglomeration without any ultrasonication or washing steps was possible due to the partial dissolution of the IONPs. The more CA solution was added, the more IONPs dissolved, however, the IONP solution pH changed only marginally. Due to this buffering effect of the IONPs, the pH of the synthesised IONP solution was independent of the amount of CA fed and stayed constant at *ca.*  $\text{pH}_{\text{IONP-sol}} = 7$  (till complete IONP dissolution).

Independently of the CA quantity fed, the IONP diameter changed only marginally and stayed around 7 nm (which corresponds to about three times the volume of 5 nm particles). We envisioned that an earlier addition of the CA solution (before IONP growth is completed) could initiate the partial dissolution of IONPs formed or possible intermediates, hindering the particles from growing further. Therefore, a CA solution was fed *via* a second T-mixer, just after initiating the CP. In order to find the optimum time to quench IONP growth, *i.e.*, just after magnetite/maghemite formation (within seconds after initiating CP),<sup>44</sup> the PTFE tube length between the first and second T-mixer was adapted to quench after 0.5 s, 2 s, 5 s, (see Fig. 1a) or 100 s. In the following, “magnetite” is used to refer to magnetite/maghemite mixtures, since an accurate differentiation between magnetite and maghemite is not possible with the diffraction-based characterisation and imaging methods used.

**Step 3: Aging.** After adding the CA solution, the solution with the precipitates passed through a coiled flow inverter (coiled PTFE tubing with flow inversions every four turns) with



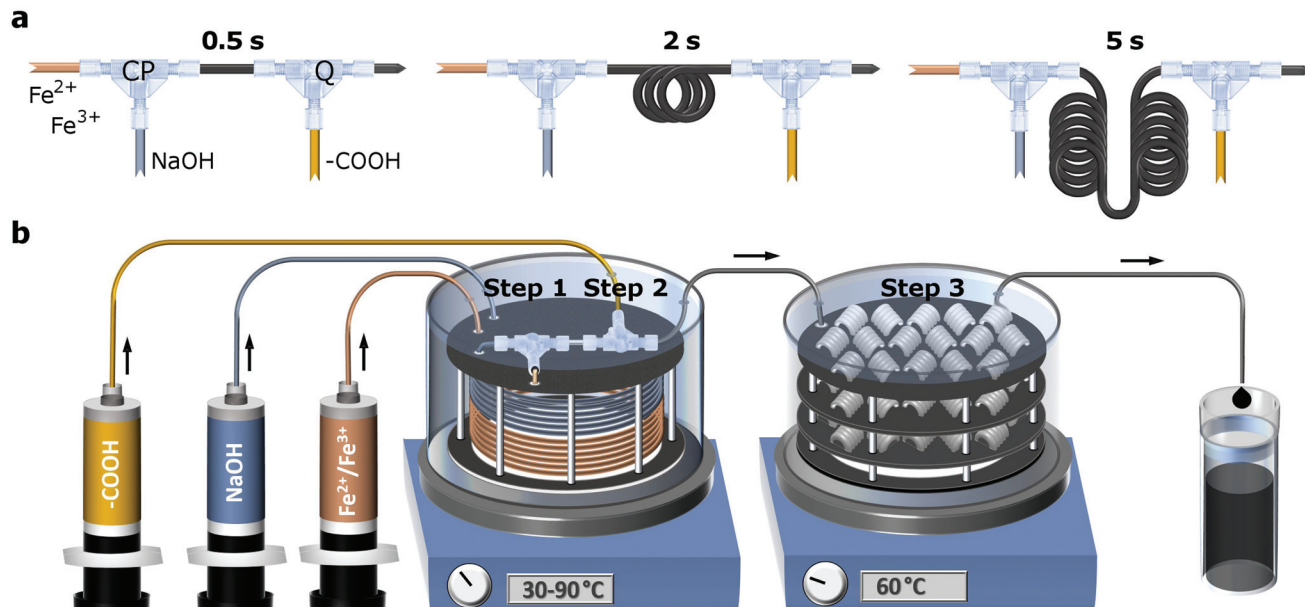


Fig. 1 Schematic of (a) precisely-timed quenching (Q) of particle growth after 0.5 s, 2 s and 5 s after initiation of co-precipitation (CP) and (b) multi-stage flow reactor to initiate co-precipitation (step 1), quenching and stabilisation (step 2, here after 0.5 s) and aging (step 3).

a total residence time of 160 s before collection, as described previously.<sup>44</sup>

The three steps could be performed at different but well defined temperatures (30–90 °C) due to the modular reactor design. The temperature was controlled by magnetically stirred water baths, into which the reactor elements were immersed to guarantee uniform conditions. For all flow syntheses 60 °C was used for step 3. A schematic of the entire flow set-up is shown in Fig. 1b. The details of the reactor components used including geometries, materials, and part numbers/manufacturers are provided in Table S2.<sup>†</sup>

### Characterisation

The hydrodynamic diameter  $D_h$  was obtained at 22 °C via dynamic light scattering (DelsaMax-Pro, Beckman Coulter). Samples were diluted with DI water up to the point where the  $D_h$  plateaued (typically after a four-fold dilution). Transmission electron microscope (TEM) images were captured with a JEOL 1200 EX microscope at a 120 kV acceleration voltage. High resolution TEM (HRTEM) images were taken with a JEOL 2100 operating at 200 kV. TEM samples were prepared by dropping 20  $\mu\text{l}$  of washed IONP solution onto carbon-coated copper grids, which were then dried overnight. The washing procedure, repeated twice, included precipitation from solution with isopropyl alcohol (IPA) (2 : 1 IPA<sub>vol</sub> : sample<sub>vol</sub>) and magnetic decantation. The particle diameter refers to a circle with the same area as the polygon obtained by fitting the edges of a particle. The average diameter  $D_{\text{TEM}}$  was obtained by manually fitting polygons around at least 100 particles in ImageJ (errors refer to the standard deviation).

The concentration of Fe in the form of particles ( $\text{mg}_{\text{Fe-IONP}} \text{ ml}^{-1}$ ) was measured via microwave plasma atomic emission

spectroscopy (MP-AES) using a 4210 MP-AES (Agilent). Samples for MP-AES were washed as described above and dried before digestion in *aqua regia* (3 : 1 HCl<sub>vol</sub> : HNO<sub>3</sub> <sub>vol</sub>). After digestion, the samples were diluted with DI water (1 : 9 *aqua regia*<sub>vol</sub> : DI water<sub>vol</sub>). The percentage of Fe conversion from precursor (concentration in  $\text{mg}_{\text{Fe-sol}} \text{ ml}^{-1}$ ) to IONPs (which could be separated by the described washing procedure) was calculated as  $[(\text{mg}_{\text{Fe-IONP}} \text{ ml}^{-1}) / (\text{mg}_{\text{Fe-sol}} \text{ ml}^{-1})] \times 100$ . X-ray diffraction (XRD) patterns of washed and dried samples were recorded using a PANalytical X'Pert3 diffractometer (Malvern Instruments) equipped with a Co K $\alpha$  radiation source ( $\lambda = 0.179 \text{ nm}$ ) operated at 40 mA and 40 kV.

SAXS measurements were performed with a Ganesha SAXSlab (Xenocs) equipped with a point focus X-ray source and a 2D detector. All curves were recorded over 1 h measurement time, within 24 h after synthesis. SAXS samples were prepared by injecting the IONP solutions (as synthesised) into 1 mm borosilicate glass capillaries (Capillary Tube Supplies).

Magnetisation hysteresis cycles at 5 K and 300 K were recorded using a superconducting quantum interference device (SQUID) magnetometer (MPMS, Quantum Design). For that, dialysed IONP solutions were dried and loaded in a capsule adapted for SQUID measurements.

Thermogravimetric analysis (TGA) was performed on an SDT 600 (TA instruments), heating the dried sample from 25 to 600 °C at 5 °C min<sup>-1</sup> under air. The TGA results were used to normalise the magnetic hysteresis curves by the amount of IONP (magnetite) and Fe per g sample (see ESI 5<sup>†</sup>).

$T_1$  and  $T_2$  relaxation times of IONPs were measured on a Minispec 60 (Bruker) at 37 °C, a frequency of 60 MHz, and using magnetic field strength of 1.41 T. The longitudinal ( $r_1$  [ $\text{mM}^{-1} \text{ s}^{-1}$ ]) and transversal ( $r_2$  [ $\text{mM}^{-1} \text{ s}^{-1}$ ]) relaxivities were

obtained from a linear regression through the relaxivity and iron concentration ( $C_{\text{Fe}}$  [mM]) dependent relaxation rates  $R$  ( $=1/T$  [s $^{-1}$ ]):  $R = R_0 + rC_{\text{Fe}}$ , where  $R_0$  is the relaxation rate of the aqueous medium. The iron concentration of IONP sample solutions (which were consecutively diluted for R measurements) was quantified by  $T_1$ -relaxometry using a calibration curve for  $\text{Fe}^{3+}$  as reported previously.<sup>46,47</sup> To establish the calibration curve,  $T_1$  relaxation rates of standard solutions, *i.e.*,  $\text{Fe}(\text{III})$  nitrate ( $\text{Fe}(\text{NO}_3)_3$ ) in 2%<sub>vol</sub> nitric acid ( $\text{HNO}_3$ ), were traced as a function of  $\text{Fe}^{3+}$ . The IONP sample solutions were digested with concentrated nitric acid (*i.e.*, a strong oxidising agent) overnight to yield an  $\text{Fe}(\text{III})$  solution, and subsequently diluted with DI water to obtain a 2%<sub>vol</sub>  $\text{HNO}_3$  solution, *i.e.*, the same  $\text{HNO}_3$  concentration used for the calibration curve.  $T_1$  relaxation time measurements of the 2%<sub>vol</sub>  $\text{HNO}_3$  sample solution provided the iron concentration by comparison with the calibration curve.

## Results and discussion

### IONP flow synthesis in the presence of dextran

Following a common method to synthesise small IONPs, a macromolecule, *i.e.*, dextran, was added to the precursor solution. When feeding the CA solution at 2.1 ml min $^{-1}$  using a tube length corresponding to 100 s after initiating CP (all steps carried out at the standard reaction temperature of 60 °C), agglomerates of precipitates formed and grew on their way through the reactor. This resulted in plugging after several minutes of operation. Stable reactor operation, however, was possible when adding the CA solution using a tube length corresponding to 5 s after initiating CP. Since the precursor solution is more acidic with dextran added, the feed rate of the CA solution was reduced from 2.1 ml min $^{-1}$  (used to stabilise particles in absence of dextran<sup>44</sup>) to 1.7 ml min $^{-1}$  in order to avoid dissolving the particles completely. TEM analysis showed a small fraction of particles  $>10$  nm (Fig. 2a<sub>1</sub>) with most of the particles being too small to determine their size (Fig. 2a<sub>2</sub>). HRTEM showed that these particles had a diameter around 2 nm (see Fig. 2b). The presence of such ultra-small particles ( $\leq 3$  nm) at short process times (such as just after initiating the CP) is in line with previous reports on CP synthesis with macromolecules,<sup>26</sup> including dextran.<sup>48,49</sup>

The ultra-small particles were identified as crystalline and of the inverse spinel structure (magnetite and/or maghemite) by HRTEM analysis including electron diffraction and zone axis analysis (see Fig. 2b and c). This agrees with the XRD pattern showing only peaks characteristic for the inverse spinel structure (see Fig. S1†). The low conversion obtained of 35% (0.85 mg $_{\text{Fe-IONP}}$  ml $^{-1}$ ) is anticipated as the CA solution was shown to dissolve  $\sim$ 50% of the IONPs at this CA flow rate.<sup>44</sup>

SAXS analysis indicated highly aggregated/agglomerated structures, as the SAXS curve follows a power law function, (see Fig. S11b†). The formation of aggregated structures in the presence of dextran is consistent with the measured hydrodynamic diameter  $D_h = 60$  nm (which is much larger than the structures seen *via* TEM). The continuation of this agglomeration when quenching after 100 s (instead of 5 s) is what caused reactor plugging.

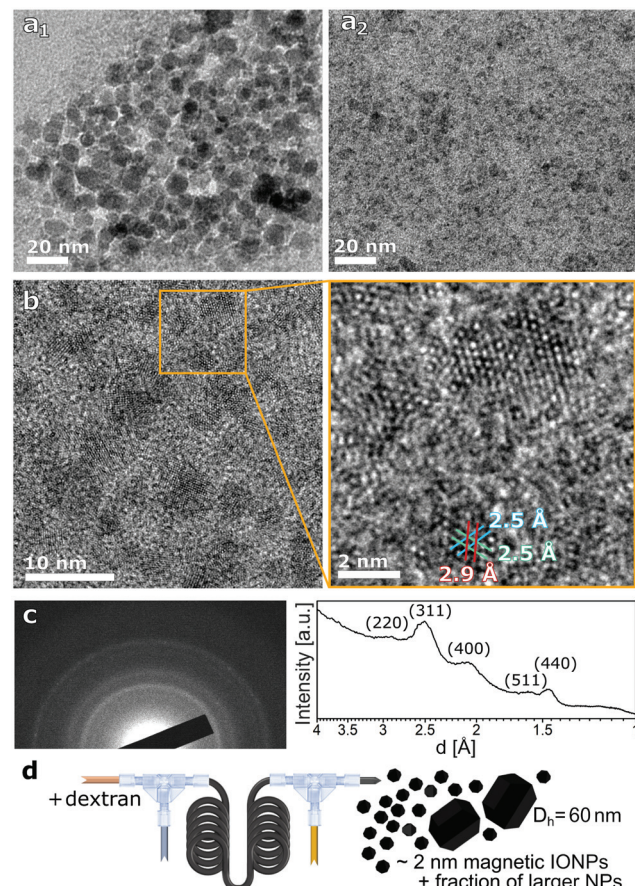


Fig. 2 Analysis of IONPs synthesised with dextran in the precursor solution and quenching 5 s after initiating co-precipitation. (a) TEM images of small fraction of particles  $>10$  nm (a<sub>1</sub>) and ultra-small IONPs (a<sub>2</sub>). (b) HRTEM image of ultra-small IONPs with a higher magnification image matching the [111] zone axes of magnetite with the two 2.5 Å (113) planes and one 2.9 Å (220) plane. (c) Electron diffraction pattern (of the area in Fig. 2b) and the radially averaged diffraction profile matching the pattern of magnetite (PDF ref. 03-065-3107). (d) Schematic of flow synthesis in the presence of dextran.

amic diameter  $D_h = 60$  nm (which is much larger than the structures seen *via* TEM). The continuation of this agglomeration when quenching after 100 s (instead of 5 s) is what caused reactor plugging.

### IONP flow synthesis with different quenching times

As explained for step 2 when describing the reactor operation, the CP synthesis yields magnetite particles within seconds. Hence, the CA solution was fed 0.5 s, 2 s and 5 s after initiating CP (*i.e.*, mixing the base and precursor solution without dextran at the standard reaction temperature of 60 °C) to find the optimum time to quench IONP growth. The synthesis with the shortest quenching time (0.5 s) yielded a dilute brownish solution when exiting the second T-mixer, as observed previously when excess CA was used for stabilisation.<sup>44</sup> Hence, the CA solution flow rate was reduced to 1.9 ml min $^{-1}$ . Still, the sample appeared reddish and separation *via* magnetic decan-



tation (after precipitation out of solution with IPA) was challenging. This suggested the presence of phases other than the magnetic inverse spinel structure. The intermediate particles reported for CP syntheses were shown to be amorphous and significantly larger than the final IONPs (of the inverse spinel structure).<sup>45,50</sup> This is in agreement with the large hydrodynamic diameter ( $D_h = 90$  nm) and the XRD pattern showing no evidence of another crystalline phase (see green line in Fig. 3a). The XRD pattern corresponding to a quenching time of 0.5 s shows no clear indication for crystalline phases, besides the broad peaks for magnetite.

For a quenching time of 2 s with the standard CA solution feed rate of  $2.1 \text{ ml min}^{-1}$ , no problem in terms of excessive particle dissolution was found. The collected solution had the expected black colour and it was a highly stable colloid with a conversion of 42% ( $0.98 \text{ mg}_{\text{Fe-IONP}} \text{ ml}^{-1}$ ). The  $D_h$  dropped to 29 nm and the XRD showed the peaks expected for inverse

spinel IONPs (see red line in Fig. 3a). Still, TEM analysis revealed, besides the expected particles in the range of 4–6 nm (see Fig. 3c<sub>1</sub>), larger structures of a different appearance (see Fig. 3c<sub>2-3</sub>).

When quenching after 5 s with a feed of  $2.1 \text{ ml min}^{-1}$  CA solution, the conversion remained at 42% and peaks of the XRD pattern became even more pronounced (see blue line in Fig. 3a). TEM analysis showed only the expected small IONPs (see Fig. 3e). The  $D_h$  dropped further to 19 nm, which is in good agreement with the particle dimensions determined by SAXS analysis ( $D_{\text{SAXS}} = 10.3$  nm, see Table S3†). As the IONP diameters obtained *via* TEM are similar, this proves that agglomeration is marginal. HRTEM revealed that these IONPs were single crystalline inverse spinel structure of magnetite (see Fig. 3f).

The magnetisation hysteresis confirmed that the IONPs were superparamagnetic (see Fig. 3g) with coercivities

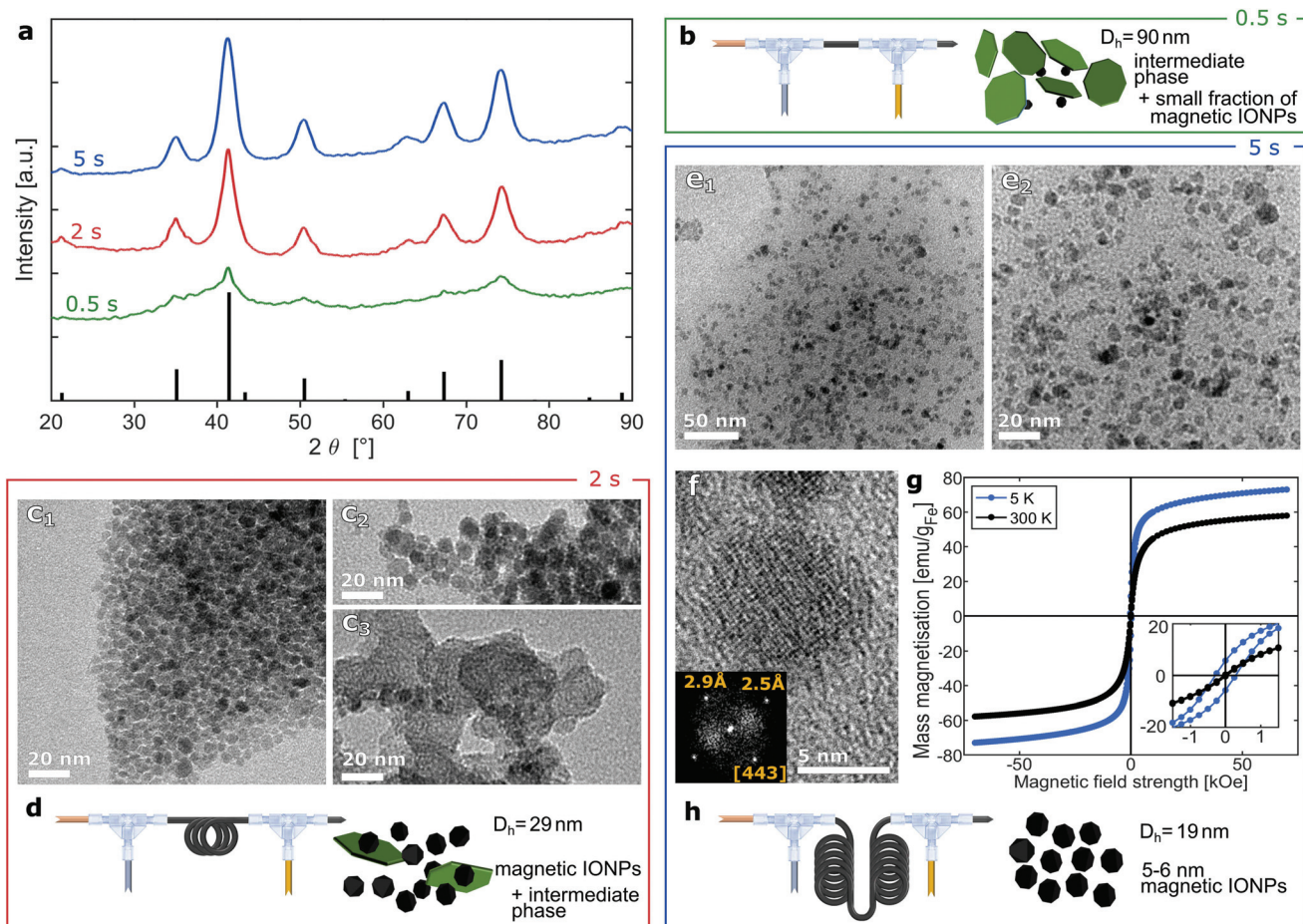


**Fig. 3** Analysis of IONPs synthesised with quenching at 0.5, 2 and 5 s after initiating co-precipitation. (a) XRD pattern. The black bars at the bottom reference the pattern of the inverse spinel structure (magnetite: PDF ref. 03-065-3107). Fig. S2† shows the overlaid patterns (including the one for quenching at 100 s). (b) Schematic of flow synthesis with quenching at 0.5 s. (c<sub>1-3</sub>) TEM images of IONPs synthesised with quenching at 2 s,  $D_{\text{TEM}} = 4.6 \pm 1.0$  nm (analysing only particles that were assumed to be magnetite based on contrast, size and shape). Fig. S3† shows the particle size distribution. (d) Schematic of flow synthesis with quenching at 2 s. (e<sub>1-2</sub>) TEM images (of different magnifications) of small IONPs synthesised with quenching at 5 s,  $D_{\text{TEM}} = 5.3 \pm 0.9$  nm. Fig. S4† shows the particle size distribution. (f) HRTEM image of IONPs synthesised with quenching at 5 s. The inset shows the FFT analysis confirming the inverse spinel structure viewed down the [443] zone axis. (g) Magnetisation hysteresis curves of IONPs synthesised with quenching at 5 s. (h) Schematic of flow synthesis with quenching at 5 s.

<0.3 kOe at 5 K and <0.04 kOe at 300 K. The saturation mass magnetisations at 300 K of 30 emu per g dialysed and dried IONPs was normalised by the IONP weight fraction of 70% determined *via* TGA (see Fig. S12†) yielding 58 emu g<sub>Fe</sub><sup>-1</sup> assuming IONPs were magnetite only (see eqn (S3)†). As expected, these values are significantly below the bulk magnetisation (103 and 128 emu g<sub>Fe</sub><sup>-1</sup> for maghemite and magnetite)<sup>51</sup> as surface effects cause a strong reduction in the magnetisation of such small IONPs. These surface effects cause different spin-ordering at the surface layer reducing the average magnetic moment.<sup>52,53</sup>

The reproducibility of this small IONPs flow synthesis was proven by repeating the synthesis with quenching after 5 s feeding CA solution at 2.1 ml min<sup>-1</sup> (as used above) and at 1.9 ml min<sup>-1</sup> and quenching after 100 s (as used previously). TEM analysis showed  $D_{\text{TEM}} = 5.4 \pm 0.8$  nm (see Fig. S7 and S10†),  $D_{\text{TEM}} = 5.5 \pm 1.0$  nm (see Fig. S8 and S10†), and  $D_{\text{TEM}} = 7.0 \pm 1.0$  nm (see Fig. S9 and S10†) respectively. In addition, a batch study was performed for comparison (see ESI 6†). It was shown that a batch synthesis can also yield small IONPs when using small volumes. The small IONPs obtained in batch, however, were aggregated and more polydisperse (see Fig. S13 and S14†). This was assigned to higher spatial inhomogeneity of temperature, pH, and reagent concentrations, hence, co-precipitation, quenching and stabilisation occurred at less uniform conditions in batch. Also, scale-up in batch is challenging, as the precisely timed quenching after seconds and required mixing time can hardly be achieved for batch volumes larger than 10 ml.<sup>54,55</sup>

### IONP flow synthesis at different temperatures

Although there is no universal correlation between the size of co-precipitated IONPs and the reaction temperature, the temperature is known to affect the size.<sup>26,56,57</sup> The temperature dependence was studied by initiating CP and quenching after 5 s (*i.e.*, synthesis steps 1 and 2) at 30 °C and 90 °C, but keeping the standard reaction temperature of 60 °C for aging (*i.e.*, step 3). When performing step 1 and 2 at 30 °C, the CA solution feed rate of 2.1 ml min<sup>-1</sup> caused significant dilution of the formed precipitates. Reducing the CA solution flow rate to 1.7 ml min<sup>-1</sup> led to a stable colloid, and the darker colour suggested an increased particle concentration. The collected solutions, however, appeared “reddish” and a significant fraction of particles could not be separated *via* magnetic decantation after precipitation out of solution. The  $D_h$  of 55 nm indicated different particle formation kinetics compared to operation at 60 °C, *i.e.*, magnetite formation is not completed after 5 s (see Fig. 4a).

Operation of steps 1 and 2 at 90 °C yielded stable IONPs solutions at the standard CA solution feed rate of 2.1 ml min<sup>-1</sup>. The TEM images (see Fig. 4b), showed relatively monodisperse IONPs with a  $D_{\text{TEM}} = 6.1 \pm 0.9$  nm. The obtained conversion was 41% (0.96 mg<sub>Fe-IONP</sub> ml<sup>-1</sup>) and the  $D_h$  was 19 nm.

Although the flow reactor was operated in single phase mode it was robust against plugging and fouling for all experiments performed except the dextran studies. This was attribu-

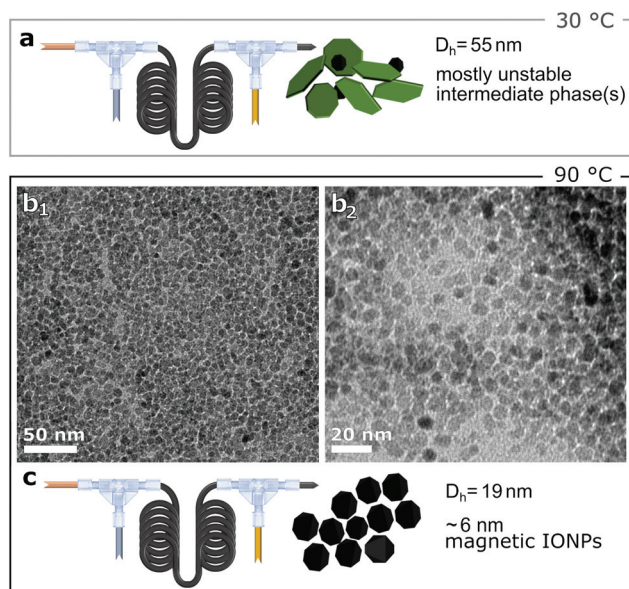


Fig. 4 (a) Schematic of flow synthesis with co-precipitation performed at 30 °C. (b<sub>1-2</sub>) TEM images of IONPs synthesised with co-precipitation performed at 90 °C,  $D_{\text{TEM}} = 6.1 \pm 0.9$  nm. (c) Schematic of flow synthesis with co-precipitation initiated at 90 °C. Fig. S5† shows the particle size distribution. For both temperatures, quenching was performed at 5 s.

ted to the T-mixers' geometry (no edges or grooves where encrustation is likely), the shear forces due to relatively high flow rates, as well as the highly negative zeta potential values of the PTFE tubing and PTFE like T mixer (see Table S2†) used in alkaline solutions.<sup>58</sup> The pH only dropped to neutral values after CA addition, hence, after IONPs (or intermediates) formed.

### Discussion of quenching mechanism

The results of the quenching studies performed at different times and temperatures strongly suggest the formation of poorly crystalline intermediates after initiating CP. These intermediates accompany the formation of the spinel phase (magnetite/maghemite) in the first seconds of the CP synthesis. The presence of such intermediates (*e.g.*, ferrihydrite or green rusts) transforming into the inverse spinel phase is well documented for CP syntheses using a weak base or a strong base which is added slowly.<sup>45,50,59,60</sup> Our results indicate that for the CP synthesis used, where a strong base is added rapidly, this transition occurs within ~3 s at 60 °C and progresses slower at 30 °C. The solubility of intermediate phases at neutral or acidic pH values is higher than that of magnetite.<sup>60,61</sup> Therefore, these intermediate phases (also referred to as nanometre-sized primary particles of amorphous iron-rich precursors)<sup>62</sup> are more likely to dissolve, or dissolve faster, when feeding the CA solution. The growth of the spinel phase is understood to be a reaction-limited process, where the primary particles supply ferrous and ferric iron.<sup>45,59,62,63</sup> Hence, stopping this supply would quench the growth of iron oxide nanoparticles.

For CA, its chelating organic anions have been reported to (i) prevent nucleation due to the chelation of iron ions<sup>64</sup> and (ii) to inhibit growth due to the adsorption on IONP nuclei, with the latter being dominant.<sup>23</sup> For example, a reduction of the IONP size to 6 nm and smaller was observed when adding citric acid to the precursor solution.<sup>23,65</sup> Chelating ligands certainly affect the IONP size,<sup>66</sup> but using CA solution is unlikely the only reason for the quenching, as it was fed after the initiation of CP, and after the formation of spinel iron oxide. Furthermore, quenching with a HCl instead of a CA solution 5 s and 100 s after initiating CP reduced the IONP size likewise, as indicated by XRD (see Fig. S6†). CA, however, was essential for the IONP stability at neutral pH.<sup>44,67</sup> More generally, quenching nanoparticle growth by rapid pH change can not only yield small IONPs *via* precipitation methods, but also small noble metal nanoparticles (synthesised in water). What these methods have in common is a nucleation step followed by a pH sensitive growth step involving either intermediate phases,<sup>68,69</sup> colloidal growth,<sup>70,71</sup> or surface mediated growth (or combinations).<sup>72–74</sup> Thermal decomposition syntheses of IONPs and other nanomaterials can be quenched by adding a coolant (such as the solvent used) to stop the decomposition reaction or temperature induced colloidal growth.<sup>75–78</sup> Although these aqueous and non-aqueous syntheses require minutes to hours for the nanoparticles to reach their final size, their formation can occur within seconds<sup>39,79,80</sup> or less.<sup>71,81</sup> Other examples are polymeric particles formed *via* radical polymerization<sup>82</sup> facilitating size control by quencher addition. Therefore, the rapid quenching facilitated by flow reactors is a unique tool to synthesise small nanoparticles.

### Evaluation of MRI contrast performance

The IONP solutions synthesised at 60 °C with quenching times of 2, 5 and 100 s (*i.e.*, the previous procedure<sup>44</sup>), and the one synthesised at 90 °C with quenching after 5 s (all quenched *via* a 2.1 ml min<sup>-1</sup> citric acid solution feed) were evaluated for MRI performance (see Fig. 5). IONPs synthesised in the presence of dextran were not considered (despite producing IONPs of  $D_{\text{TEM}} \sim 2$  nm) due to the bimodal IONP size distribution (indicating different particle formation mechanisms, which are likely to cause scalability issues) and the larger hydrodynamic diameter indicating agglomeration.

Unreacted iron precursor and other reagents were removed from solution by dialysing against DI water using a 12–14 kDa membrane (Medicell) over 4 d, while changing the water frequently. The Fe concentrations ( $C_{\text{Fe}}$ ) of the dialysed IONP solutions were 7.7 mM, 7.9 mM, and 6.7 mM (CP at 60 °C, quenching time 100 s, 5 s, and 2 s respectively), and 6.7 mM (precipitated at 90 °C and quenched after 5 s). The relaxation rates ( $1/T$ ) dependence on the Fe concentration used to determine the relaxivities are shown in Fig. 5b. Table 1 compares the relaxivities of the four studied IONP samples and their sizes.

The transversal relaxivities ( $r_2$ ) scaled with the IONP size from the lowest of 20.5 mM<sup>-1</sup> s<sup>-1</sup> to the highest of 57.2 mM<sup>-1</sup> s<sup>-1</sup> for IONPs quenched 2–100 s after initiating CP. This is

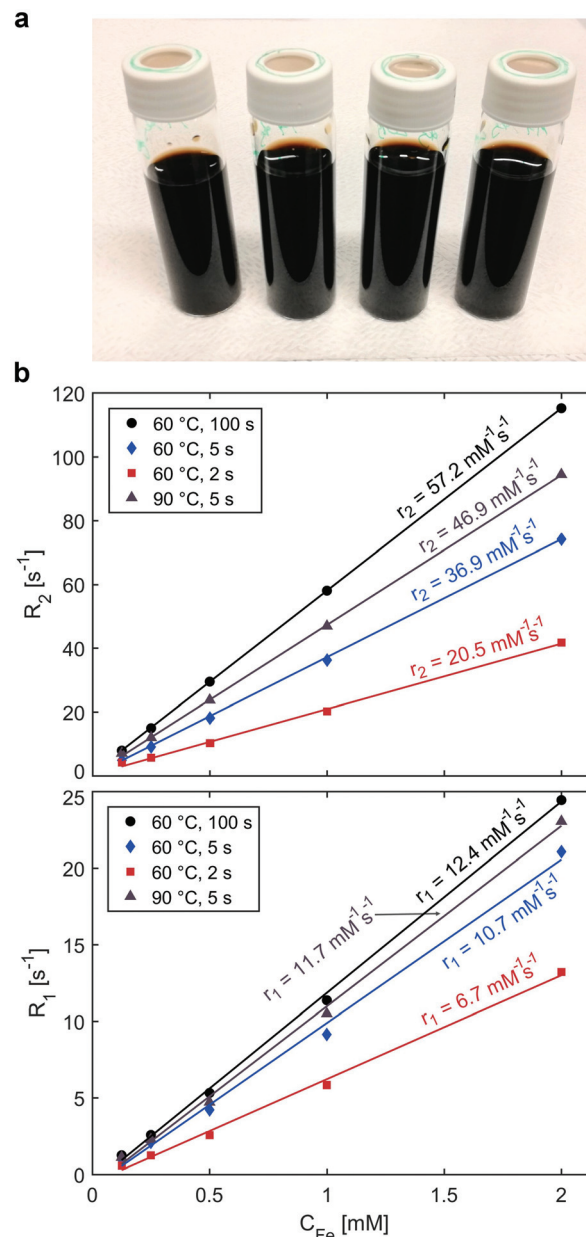


Fig. 5 (a) IONP solutions synthesised with quenching times of 100, 5 and 2 s at 60 °C and 5 s at 90 °C (from left to right) selected for MRI contrast performance evaluation. (b) Relaxation rates  $R_2$  (transversal, top) and  $R_1$  (longitudinal, bottom) vs. iron concentration in the (consecutively diluted) dialysed samples ( $C_{\text{Fe}}$ ) to determine  $r_1$  and  $r_2$  (*i.e.*, the slope) for IONPs synthesised at co-precipitation temperatures and quenching times as indicated.

expected as  $r_2$  depends on the magnetic moment, which is higher for larger particles, as the reduction of magnetisation due to surface effects becomes less prominent with increasing size.

Although the longitudinal relaxivities ( $r_1$ ) also correlated with the IONP size, the highest values of 10.7, 12.4, and 11.7 mM<sup>-1</sup> s<sup>-1</sup> (for IONPs precipitated at 60 °C and quenched after 5 s and 100 s, and precipitated at 90 °C and quenched

**Table 1** Nanoparticle diameters,  $D_{\text{TEM}}$ ,  $D_h$ , and longitudinal ( $r_1$ ) and transversal ( $r_2$ ) relaxivities (measured at 37 °C, 60 MHz and 1.41 T) of selected IONP samples (all quenched with 2.1 ml min<sup>-1</sup> CA solution)

Synthesised at:					
Co-prec. temperature	Quenching time	$D_{\text{TEM}}/D_h$ [nm]	$r_1$ [mM <sup>-1</sup> s <sup>-1</sup> ]	$r_2$ [mM <sup>-1</sup> s <sup>-1</sup> ]	$r_2/r_1$ [—]
60 °C	100 s	6.9/19	12.4	57.2	4.6
60 °C	5 s	5.4/19	10.7	36.9	3.4
60 °C	2 s	4.6/29	6.7	20.5	3.0
90 °C	5 s	6.1/19	11.7	46.9	4.0

after 5 s respectively) are comparable. Longitudinal relaxivities  $>10$  mM<sup>-1</sup> s<sup>-1</sup> have been previously reported for IONPs produced using thermal decomposition methods.<sup>5,13,14,83–85</sup> Ours, however, are among the highest values achieved *via* a water-based IONP synthesis, hence, without organic solvents.<sup>6,8</sup> These high relaxivities are attributed to the large accessible surface of the non-agglomerated, colloidally stable, and small IONPs synthesised, maximising the water-Fe interfacial area. Also, the stabilisation with CA, *i.e.*, a small molecule with a molecular weight  $<200$  g mol<sup>-1</sup>, is expected to be pivotal. Citric acid is not only biocompatible but also allows the water molecules to approach the superparamagnetic IONPs and was shown in the past to enable high  $r_1$  values.<sup>13,31,86</sup>

Besides a comparison with IONPs developed as  $T_1$  contrast agents, it is relevant to compare the  $r_1$  and  $r_2$  values with superparamagnetic IONPs developed as  $T_2$  contrast agents in the literature. Such IONPs usually have a magnetic core size in the range of 10–20 nm,  $r_2$  values in the range 80–300 mM s<sup>-1</sup>, (depending on the design, the shape and the organic coating) and  $r_1$  values around 10 mM<sup>-1</sup> s<sup>-1</sup>.<sup>83,84</sup> Therefore, compared to IONP  $T_2$ -agents, the MRI features of the small IONP synthesised in flow have several times lower  $r_2$  value, while  $r_1$  remains similar, which allows to decrease the  $r_2/r_1$  ratio, a favoured parameter for  $T_1$ -MRI.<sup>85</sup> Especially the small IONPs synthesised (quenched at 5 s, standard reaction temperature of 60 °C) exhibit a high  $r_1$  value (10.7 mM<sup>-1</sup> s<sup>-1</sup>) with a comparatively low  $r_2$  value ( $r_2/r_1 = 3.4$ ).

These  $r_1$  values are also significantly higher than those of Gd complexes used commercially in  $T_1$ -MRI, *e.g.*, macrocyclic Gd complexes such as Dotarem® and Gadovist®, which have  $r_1$  values of 4.2 mM<sup>-1</sup> s<sup>-1</sup> and 5.3 mM<sup>-1</sup> s<sup>-1</sup> (at 1.5 T and 37 °C) respectively.<sup>87</sup>

## Conclusions

We have showcased a flow synthesis of nanoparticles benefiting from the efficient heat transfer and rapid mixing of flow reactors, but most importantly, precisely timed reagent addition. Such addition, feasible in flow reactors, enables excellent control during the crucial particle formation stage for nanoparticle syntheses with rapid kinetics (within seconds).

We have used this principle to quench the growth of IONPs during a fast co-precipitation synthesis. A multistage flow reactor was used to (i) initiate co-precipitation and (ii) feed an acid solution after the formation of magnetite/maghemitic IONPs to stop their growth. Growth quenching was rationalised by the (at least partial) dissolution of intermediate phases before their transition to the inverse spinel structure (magnetite/maghemitic); hence, stopping the supply of ferrous and/or ferric ions to form these intermediates. To synthesise small IONPs ( $\leq 5$  nm) required for  $T_1$  MRI contrast agents, particle growth had to be quenched just after the formation of magnetite.

The XRD patterns, TEM studies, hydrodynamic diameters and SAXS curves of IONPs synthesised with quenching times between 0.5 and 100 s show that formation of the inverse spinel structure occurs between 0.5 and 2 s for the synthesis used (NaOH solution added rapidly to a precursor solution of ferric and ferrous chlorides at 60 °C). Quenching the growth significantly later did allow particles to grow larger than 5 nm, whereas premature acid addition yielded undesired oxide phases. Furthermore, temperature affected the reaction kinetics, *i.e.*, lower temperatures delayed the formation of magnetite/maghemitic IONPs. When quenching 5 s after initiating CP, the synthesis at 30 °C did not show a high magnetite yield, whereas the synthesis at 60 °C and 90 °C resulted in 5.4 nm and 6.1 nm magnetite particles respectively at precursor conversions of 41–42%.

This flow chemistry protocol facilitated the reproducible production of stable and only marginally agglomerated small IONPs coated with CA at neutral pH values without any toxic reagent. Furthermore, the short synthesis time of the CP method used, and the continuous operation of the flow reactor allows for reproducible production at larger scales ( $>15$  l d<sup>-1</sup> with  $\sim 1$  g<sub>Fe-IONP</sub> l<sup>-1</sup>, for the 5 ml min<sup>-1</sup> NaOH and precursor solution flow rates used) with a simple lab-scale set-up (no parallelisation, no flow rate increase, *etc.*). A comparison with batch showed that IONPs produced in flow are more monodisperse, indicating the challenges of batch scale-up.

Our synthesis procedure entails a raw materials cost  $<\text{£}10$  per g<sub>Fe-IONP</sub> (calculated based on the yield of  $\sim 1$  g<sub>Fe-IONP</sub> l<sup>-1</sup> and costs for precursors, CA and NaOH). Despite the slightly higher equipment costs for flow reactors, *e.g.* for pumps, this difference is insignificant when comparing the total costs of batch and flow nanoparticle production, as shown recently.<sup>88</sup>

Relaxometric studies revealed the potential of these small IONPs as positive ( $T_1$ ) contrast agents for MRI. The  $r_1$  values obtained were larger than 10 mM<sup>-1</sup> s<sup>-1</sup> (with  $r_2/r_1 \leq 4$ ), which is among the highest values reported for water-based syntheses.

## Conflicts of interest

There are no conflicts to declare.



## Acknowledgements

The authors thank the EPSRC for financial support (EP/M015157/1) through the Manufacturing Advanced Functional Materials (MAFuMa) scheme. NTKT thanks AOARD (FA2386-17-1-4042 award) for funding. LP was supported by the European Union's Horizon 2020 research and innovation programme under the Marie Skłodowska-Curie grant agreement no. 721290. This publication reflects only the author's view, exempting the Community from any liability. Project website: <http://cosmic-etc.eu/>. This work was carried out in part through the use of the INL Advanced Electron Microscopy, Imaging and Spectroscopy Facility.

## References

- 1 M. Le Fur and P. Caravan, *Metalloomics*, 2019, **11**, 240–254.
- 2 Q. Feng, Y. Liu, J. Huang, K. Chen, J. Huang and K. Xiao, *Sci. Rep.*, 2018, **8**, 2082.
- 3 G. Cotin, S. Piant, D. Mertz, D. Felder-Flesch and S. Begin-Colin, in *Iron Oxide Nanoparticles for Biomedical Applications*, Elsevier, Amsterdam, 2018, pp. 43–88.
- 4 R. Hachani, M. A. Birchall, M. W. Lowdell, G. Kasparis, L. D. Tung, B. B. Manshian, S. J. Soenen, W. Gsell, U. Himmelreich, C. A. Gharagouzloo, S. Sridhar and N. T. K. Thanh, *Sci. Rep.*, 2017, **7**, 7850.
- 5 H. Wei, O. T. Bruns, M. G. Kaul, E. C. Hansen, M. Barch, A. Wiśniowska, O. Chen, Y. Chen, N. Li, S. Okada, J. M. Cordero, M. Heine, C. T. Farrar, D. M. M. Montana, G. Adam, H. Ittrich, A. Jasano, P. Nielsen and M. G. Bawendi, *Proc. Natl. Acad. Sci. U.S.A.*, 2017, **114**, 2325–2330.
- 6 Y. Bao, J. A. Sherwood and Z. Sun, *J. Mater. Chem. C*, 2018, **6**, 1280–1290.
- 7 C. Tao, Q. Zheng, L. An, M. He, J. Lin, Q. Tian and S. Yang, *Nanomaterials*, 2019, **9**, 170.
- 8 B. Chen, Z. Guo, C. Guo, Y. Mao, Z. Qin, D. Ye, Z. Fengchao, Z. Lou, Z. Zhang, M. Li, Y. Liu, M. Ji, J. Sun and N. Gu, *Nanoscale*, 2020, **12**, 5521–5532.
- 9 J. K. Oh and M.-A. Fortin, in *Clinical Applications of Magnetic Nanoparticles*, ed. N. T. K. Thanh, CRC Press, Taylor & Francis, Boca Raton, London, New York, 2018, pp. 139–160.
- 10 Z. Zhou, L. Yang, J. Gao and X. Chen, *Adv. Mater.*, 2019, **31**, 1804567.
- 11 J. Wan, R. Yuan, C. Zhang, N. Wu, F. Yan, S. Yu and K. Chen, *J. Phys. Chem. C*, 2016, **120**, 23799–23806.
- 12 M. Mahmoudi and S. Laurent, *Iron Oxide Nanoparticles for Biomedical Applications: Synthesis, Functionalization and Application*, Elsevier, Amsterdam, 1st edn, 2017.
- 13 E. Taboada, E. Rodríguez, A. Roig, J. Oró, A. Roch and R. N. Muller, *Langmuir*, 2007, **23**, 4583–4588.
- 14 F. Hu, Q. Jia, Y. Li and M. Gao, *Nanotechnology*, 2011, **22**, 245604.
- 15 S. Sun and H. Zeng, *J. Am. Chem. Soc.*, 2002, **124**, 8204–8205.
- 16 U. I. Tromsdorf, O. T. Bruns, S. C. Salmen, U. Beisiegel and H. Weller, *Nano Lett.*, 2009, **9**, 4434–4440.
- 17 M. Z. Iqbal, X. Ma, T. Chen, L. Zhang, W. Ren, L. Xiang and A. Wu, *J. Mater. Chem. B*, 2015, **3**, 5172–5181.
- 18 Q. Dong, Z. Meng, C. L. Ho, H. Guo, W. Yang, I. Manners, L. Xu and W. Y. Wong, *Chem. Soc. Rev.*, 2018, **47**, 4934–4953.
- 19 S. Xiao, X. Yu, L. Zhang, Y. Zhang, W. Fan, T. Sun, C. Zhou, Y. Liu, Y. Liu, M. Gong and D. Zhang, *Int. J. Nanomed.*, 2019, **14**, 8499–8507.
- 20 F. Hu, K. W. MacRenaris, E. A. Waters, T. Liang, E. A. Schultz-Sikma, A. L. Eckermann and T. J. Meade, *J. Phys. Chem. C*, 2009, **113**, 20855–20860.
- 21 R. Massart, *IEEE Trans. Magn.*, 1981, **17**, 1247–1248.
- 22 A. A. Olowe and J. M. R. Génin, *Corros. Sci.*, 1991, **32**, 965–984.
- 23 A. Bee, R. Massart and S. Neveu, *J. Magn. Magn. Mater.*, 1995, **149**, 6–9.
- 24 K. Kumar, A. M. Nightingale, S. H. Krishnadasan, N. Kamaly, M. Wylenzinska-Arridge, K. Zeissler, W. R. Branford, E. Ware, A. J. deMello and J. C. deMello, *J. Mater. Chem.*, 2012, **22**, 4704.
- 25 Z. Li, P. W. Yi, Q. Sun, H. Lei, H. Li Zhao, Z. H. Zhu, S. C. Smith, M. B. Lan and G. Q. M. Lu, *Adv. Funct. Mater.*, 2012, **22**, 2387–2393.
- 26 B. Chen, Z. Guo, C. Guo, Y. Mao, Z. Qin, D. Ye, F. Zang, Z. Lou, Z. Zhang, M. Li, Y. Liu, M. Ji, J. Sun and N. Gu, *Nanoscale*, 2020, **12**, 5521–5532.
- 27 B. Chen, J. Sun, F. Fan, X. Zhang, Z. Qin, P. Wang, Y. Li, X. Zhang, F. Liu, Y. Liu, M. Ji and N. Gu, *Nanoscale*, 2018, **10**, 7369–7376.
- 28 J.-M. Lim, A. Swami, L. M. Gilson, S. Chopra, S. Choi, J. Wu, R. Langer, R. Karnik and O. C. Farokhzad, *ACS Nano*, 2014, **8**, 6056–6065.
- 29 M. Fang, V. Ström, R. T. Olsson, L. Belova and K. V. Rao, *Nanotechnology*, 2012, **23**, 145601.
- 30 F. Haseidl, B. Müller and O. Hinrichsen, *Chem. Eng. Technol.*, 2016, **39**, 2051–2058.
- 31 J. Pellico, J. Ruiz-Cabello, I. Fernández-Barahona, L. Gutiérrez, A. V. Lechuga-Vieco, J. A. Enríquez, M. P. Morales and F. Herranz, *Langmuir*, 2017, **33**, 10239–10247.
- 32 I. Fernández-Barahona, L. Gutiérrez, S. Veintemillas-Verdaguer, J. Pellico, M. D. P. Morales, M. Catala, M. A. Del Pozo, J. Ruiz-Cabello and F. Herranz, *ACS Omega*, 2019, **4**, 2719–2727.
- 33 J. E. M. Allan, *Technology Transfer in Nanotechnology*, Publications Office of the European Union, Luxembourg, 2019.
- 34 R. Bawa, G. F. Audette and B. E. Reese, *Handbook of Clinical Nanomedicine: Law, Business, Regulation, Safety, and Risk*, Pan Stanford Publishing Pte. Ltd., Boca Raton, 2016.
- 35 X. Z. Lin, A. D. Terepka and H. Yang, *Nano Lett.*, 2004, **4**, 2227–2232.
- 36 J. Wagner and J. M. Köhler, *Nano Lett.*, 2005, **5**, 685–691.
- 37 O. Długosz and M. Banach, *React. Chem. Eng.*, 2020, **5**, 1619–1641.



38 B. Pinho and L. Torrente-Murciano, *React. Chem. Eng.*, 2020, **5**, 342–355.

39 L. Uson, M. Arruebo, V. Sebastian and J. Santamaria, *Chem. Eng. J.*, 2018, **340**, 66–72.

40 M. James, R. A. Revia, Z. Stephen and M. Zhang, *Nanomaterials*, 2020, **10**, 1–19.

41 L. Panariello, G. Wu, M. O. Besenhard, K. Loizou, L. Storozhuk, N. T. K. Thanh and A. Gavrilidis, *Materials*, 2020, **13**, 1019.

42 J. Mahin and L. Torrente-Murciano, *Chem. Eng. J.*, 2020, **396**, 125299.

43 A. Abou-Hassan, O. Sandre, V. Cabuil and P. Tabeling, *Chem. Commun.*, 2008, 1783.

44 M. O. Besenhard, A. P. LaGrow, A. Hodzic, M. Kriechbaum, L. Panariello, G. Bais, K. Loizou, S. Damilos, M. Margarida Cruz, N. T. K. Thanh and A. Gavrilidis, *Chem. Eng. J.*, 2020, **399**, 125740.

45 A. P. LaGrow, M. O. Besenhard, A. Hodzic, A. Sergides, L. K. Bogart, A. Gavrilidis and N. T. K. Thanh, *Nanoscale*, 2019, **11**, 6620–6628.

46 S. Boutry, D. Forge, C. Burtea, I. Mahieu, O. Murariu, S. Laurent, L. Vander Elst and R. N. Muller, *Contrast Media Mol. Imaging*, 2009, **4**, 299–304.

47 F. Perton, M. Tasso, G. A. Muñoz Medina, M. Ménard, C. Blanco-Andujar, E. Portiansky, M. B. F. van Raap, D. Bégin, F. Meyer, S. Begin-Colin and D. Mertz, *Appl. Mater. Today*, 2019, **16**, 301–314.

48 K. M. Lee, S.-G. Kim, W.-S. Kim and S. S. Kim, *Korean J. Chem. Eng.*, 2002, **19**, 480–485.

49 E. A. Osborne, T. M. Atkins, D. A. Gilbert, S. M. Kauzlarich, K. Liu and A. Y. Louie, *Nanotechnology*, 2012, **23**, 215602.

50 T. Ahn, J. H. Kim, H.-M. Yang, J. W. Lee and J.-D. Kim, *J. Phys. Chem. C*, 2012, **116**, 6069–6076.

51 D. J. Dunlop and Ö. Özdemir, *Rock Magnetism*, Cambridge University Press, Cambridge, 1997.

52 A. Demortière, P. Panissod, B. P. Pichon, G. Pourroy, D. Guillou, B. Donnio and S. Bégin-Colin, *Nanoscale*, 2011, **3**, 225–232.

53 D. A. Garanin and H. Kachkachi, *Phys. Rev. Lett.*, 2003, **90**, 4.

54 R. A. Ghotli, A. A. A. Raman, S. Ibrahim and S. Baroutian, *Chem. Eng. Commun.*, 2013, **200**, 595–627.

55 M. Kordas, G. Story, M. Konopacki and R. Rakoczy, *Ind. Eng. Chem. Res.*, 2013, **52**, 13818–13828.

56 H. C. Roth, S. P. Schwaminger, M. Schindler, F. E. Wagner and S. Berensmeier, *J. Magn. Magn. Mater.*, 2015, **377**, 81–89.

57 C. Blanco-Andujar, D. Ortega, Q. A. Pankhurst and N. T. K. Thanh, *J. Mater. Chem.*, 2012, **22**, 12498.

58 H. Huang, H. Du Toit, M. O. Besenhard, S. Ben-Jaber, P. Dobson, I. Parkin and A. Gavrilidis, *Chem. Eng. Sci.*, 2018, **198**, 422–430.

59 J. Baumgartner, A. Dey, P. H. H. Bomans, C. Le Coadou, P. Fratzl, N. A. J. M. Sommerdijk and D. Faivre, *Nat. Mater.*, 2013, **12**, 310–314.

60 J.-P. Jolivet, C. Chanéac and E. Tronc, *Chem. Commun.*, 2004, **54**, 477–483.

61 U. Schwertmann and R. M. Cornell, *Iron Oxides in the Laboratory: Preparation and Characterization*, Wiley-VCH, Weinheim, 2000.

62 M. Widdrat, E. Schneck, V. Reichel, J. Baumgartner, L. Bertinetti, W. Habraken, K. Bente, P. Fratzl and D. Faivre, *J. Phys. Chem. Lett.*, 2017, **8**, 1132–1136.

63 V. Reichel and D. Faivre, in *New Perspectives on Mineral Nucleation and Growth*, Springer International Publishing, Basel, 2017, pp. 275–291.

64 T. Ishikawa, S. Kataoka and K. Kandori, *J. Mater. Sci.*, 1993, **28**, 2693–2698.

65 L. Li, K. Y. Mak, C. W. Leung, K. Y. Chan, W. K. Chan, W. Zhong and P. W. T. Pong, *Microelectron. Eng.*, 2013, **110**, 329–334.

66 S. Laurent, D. Forge, M. Port, A. Roch, C. Robic, L. Vander Elst and R. N. Muller, *Chem. Rev.*, 2008, **108**, 2064–2110.

67 M. E. De Sousa, M. B. Fernández Van Raap, P. C. Rivas, P. Mendoza Zélis, P. Girardin, G. A. Pasquevich, J. L. Alessandrini, D. Muraca and F. H. Sánchez, *J. Phys. Chem. C*, 2013, **117**, 5436–5445.

68 F. Vereda, J. de Vicente and R. Hidalgo-Alvarez, *J. Colloid Interface Sci.*, 2013, **392**, 50–56.

69 A. E. Rawlings, J. P. Bramble, A. M. Hounslow, M. P. Williamson, A. E. Monnington, D. J. Cooke and S. S. Staniland, *Chemistry*, 2016, **22**, 7885–7894.

70 R. Hufschmid, E. Teeman, B. L. Mehdi, K. M. Krishnan and N. D. Browning, *Nanoscale*, 2019, **11**, 13098–13107.

71 J. Polte, X. Tuaev, M. Wuithschick, A. Fischer, A. F. Thuenemann, K. Rademann, R. Krahnert and F. Emmerling, *ACS Nano*, 2012, **6**, 5791–5802.

72 M. Wuithschick, A. Birnbaum, S. Witte, M. Sztucki, U. Vainio, N. Pinna, K. Rademann, F. Emmerling, R. Krahnert and J. Polte, *ACS Nano*, 2015, **9**, 7052–7071.

73 J. Polte, *CrystEngComm*, 2015, **17**, 6809–6830.

74 L. Panariello, A. N. P. Radhakrishnan, I. Papakonstantinou, I. P. Parkin and A. Gavrilidis, *J. Phys. Chem. C*, 2020, **124**, 27662–27672.

75 A. Lassenberger, T. A. Grünwald, P. D. J. van Oostrum, H. Rennhofer, H. Amenitsch, R. Zirbs, H. C. Lichtenegger and E. Reimhult, *Chem. Mater.*, 2017, **29**, 4511–4522.

76 H. Chang, B. H. Kim, H. Y. Jeong, J. H. Moon, M. Park, K. Shin, S. I. Chae, J. Lee, T. Kang, B. K. Choi, J. Yang, M. S. Bootharaju, H. Song, S. H. An, K. M. Park, J. Y. Oh, H. Lee, M. S. Kim, J. Park and T. Hyeon, *J. Am. Chem. Soc.*, 2019, **141**, 7037–7045.

77 Q. Dong, G. Li, H. Wang, P. W.-T. Pong, C. W. Leung, I. Manners, C. L. Ho, H. Li and W. Y. Wong, *J. Mater. Chem. C*, 2015, **3**, 734–741.

78 H. Gavilán, E. H. Sánchez, M. E. F. Brollo, L. Asín, K. K. Moerner, C. Frandsen, F. J. Lázaro, C. J. Serna, S. Veintemillas-Verdaguer, M. P. Morales and L. Gutiérrez, *ACS Omega*, 2017, **2**, 7172–7184.

79 P. Sharma, N. Holliger, P. H. Pfromm, B. Liu and V. Chikan, *ACS Omega*, 2020, **5**, 19853–19860.



80 S. G. Kwon and T. Hyeon, *Acc. Chem. Res.*, 2008, **41**, 1696–1709.

81 J. Polte, R. Erler, A. F. Thünemann, S. Sokolov, T. T. Ahner, K. Rademann, F. Emmerling and R. Krahnert, *ACS Nano*, 2010, **4**, 1076–1082.

82 H. J. M. Wolff, M. Kather, H. Breisig, W. Richtering, A. Pich and M. Wessling, *ACS Appl. Mater. Interfaces*, 2018, **10**, 24799–24806.

83 B. Basly, G. Popa, S. Fleutot, B. P. Pichon, A. Garofalo, C. Ghobril, C. Billotey, A. Berniard, P. Bonazza, H. Martinez, D. Felder-Flesch and S. Begin-Colin, *J. Chem. Soc., Dalton Trans.*, 2013, **42**, 2146–2157.

84 X. Y. Wang, D. Mertz, C. Blanco-Andujar, A. Bora, M. Ménard, F. Meyer, C. Giraudeau and S. Bégin-Colin, *RSC Adv.*, 2016, **6**, 93784–93793.

85 C. Blanco-Andujar, A. Walter, G. Cotin, C. Bordeianu, D. Mertz, D. Felder-Flesch and S. Begin-Colin, *Nanomedicine*, 2016, **11**, 1889–1910.

86 L. Zeng, W. Ren, J. Zheng, P. Cui and A. Wu, *Phys. Chem. Chem. Phys.*, 2012, **14**, 2631–2636.

87 P. Hermann, J. Kotek, V. Kubíček and I. Lukeš, *Dalton Trans.*, 2008, 3027–3047.

88 M. Besenhard, A. LaGrow, S. Famiani, M. Pucciarelli, P. Lettieri, N. T. K. Thanh and A. Gavriilidis, *React. Chem. Eng.*, 2020, **5**, 1474.

